Heliyon 10 (2024) e24312

Contents lists available at ScienceDirect

Heliyon

journal homepage: www.cell.com/heliyon

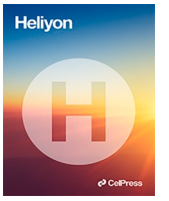

Research article

Effect of internal fractures on mechanical properties and failure of sandstone under multi-physical fields

Tianyi Shi [a,b], Jianxin Fu [a,b,*], Weidong Song [a,b], Jie Wang [a,b], Kazimi M. Y [a,b]

[a] School of Civil and Resources Engineering, University of Science and Technology Beijing, Beijing 100083, China
[b] State Key Laboratory of High-Efficient Mining and Safety of Metal Mines of Ministry of Education, University of Science and Technology Beijing, Beijing 100083, China

ARTICLE INFO

Keywords:
Multi-field coupling
Rock mechanics
Damage evolution
constitutive model

ABSTRACT

Under deep mining conditions, rocks are subjected to complex multi-physical fields and can contain numerous pores and fractures. To explore the influence and correlation of these factors on the physical and mechanical properties of fractured rock samples, this study conducted triaxial compression tests on sandstone specimens under various physical conditions using a rock full stress multi-field coupling triaxial tester. Additionally, a random fracture model for multi-field coupling numerical simulation was established. This allowed the study to obtain the mechanical parameters, failure mode, and internal fracture development of rocks under multi-physical field conditions. By analyzing the complete stress-strain curve, mechanical characteristic points, and permeability, a combination of laboratory tests and numerical simulations was used to examine how temperature, seepage, and stress fields affect the development of pores and fractures in rocks. It was found that the temperature field, under conventional geothermal conditions, generates tensile force through thermal expansion and the presence of fluid, thereby promoting fracture development within the rocks. This mechanism is similar to that of seepage. The confining pressure caused by deep geo stress uniformly inhibits the expansion of pores and fissures within the rocks.

1. Introduction

As mining depth increases, deep rock masses are subjected to more severe multi-field coupling effects in the "three high(High ground stress, high ground temperature, high karst water pressure)" environment, primarily involving temperature, mechanical, and hydraulic fields. Additionally, natural rocks often contain numerous joint fissures, which are the main causes of rock failure. Therefore, studying the development and mechanical characteristics of primary internal fractures in deep rock masses under the influence of multiple physical fields is crucial for disaster prevention and mine design in the deep mining process [1,2].

Hence, numerous researchers have conducted studies on the alteration of rock properties under the influence of multi-field coupling effects. In deep tunnel simulation experiments, it has been observed that variations in the lateral pressure coefficient can alter the stress field, subsequently affecting the movement of rock particles and changing the energy field and displacement field [3]. During high-temperature testing, it has been observed that the strength and elastic modulus of rocks decrease as the temperature rises [4,5]. A numerical simulation study on the unidirectional heating of sandstone found that during compression, the first principal stress

* Corresponding author. School of Civil and Resources Engineering, University of Science and Technology Beijing, Beijing 100083, China.
E-mail address: fujun0011@126.com (J. Fu).

https://doi.org/10.1016/j.heliyon.2024.e24312
Received 1 August 2023; Received in revised form 2 January 2024; Accepted 5 January 2024
Available online 9 January 2024

and plastic zone tended to concentrate in the high-temperature region [6]. Several scholars have proposed a heat flow coupling model that takes into account non-Darcy flow to simulate the heat transfer process in complex fractured rock masses. This model considers the flow of fluids through fractures in addition to the heat transfer, allowing for more accurate simulations in such cases [7]. The change threshold of the acoustic emission characteristics in sandstone after heating and cooling treatment has been observed to occur between 400 and 600 °C. This temperature range is where significant changes in the acoustic emission properties of sandstone are detected [8, 9]. Through research, many scholars have found that the increase and decrease in permeability correspond to different stages of rock failure [10–12]. When the relaxation stress level is at the stable and unstable development stage of rock microcracks, the increase of pore water pressure can significantly improve rock stress relaxation and radial strain change [13]. The dissipated energy density in the process of bearing rock samples increases with an increase in confining pressure. Additionally, the absolute values of various energy input densities at the same stress level increase with an increase in pore water pressure [14]. With an increase in confining pressure or effective confining pressure, the peak strength and elastic modulus of rock will increase. However, the Poisson's ratio of rock shows a downward trend. On the other hand, the effect of pore water pressure on the peak strength, elastic modulus, and Poisson's ratio of rock is opposite to that of confining pressure [15]. Some scholars have developed a new THMC (Thermo-Hydro-Mechanical-Chemical) coupling fracture criterion to predict the initiation load of brittle rocks [16]. Some scholars have also proposed an early warning signal of rock mass instability based on microseismic activity under the condition of multi-field coupling [17]. Many other scholars have developed rock damage models that take into account multi-field coupling by considering energy or damage variables [18–23].

Additionally, various scholars have investigated the modes of crack propagation in rocks under different physical conditions. Researchers recorded the acoustic emission data from rocks as their temperatures were elevated from room temperature to 500 °C and subsequently lowered. They discovered that the acoustic emission energy varied significantly among different rock types, illustrating that the thermal damage progression in rocks is highly dependent on their lithology [24]. Under hydraulic coupling conditions, the low-frequency signals of acoustic emission continuously increase, while the high-frequency signals suddenly appear intensively. This phenomenon can be used as early warning reference information for detecting overall fracture in the test piece [25]. Some researchers have used the IR count as a characterization parameter for the rock damage variable. They have established a method to quantitatively characterize the damage evolution of coal and rock by incorporating IR and stress-strain constitutive models [26]. Other researchers have investigated the evolution of the permeability coefficient of single fractured unsaturated limestone under the stress-seepage coupling field. They considered factors such as confining capillary pressure, fracture surface roughness, and the micro-fracture mode of rock under different physical fields [27–30]. In addition, some researchers have taken into account the interaction between the cracking process, hydration reaction, and heat transfer. They have proposed a concrete-heat-force multi-field coupling phase-field cohesive crack model [31]. Furthermore, there have been studies on the microscopic damage of saturated sandstone under unloading conditions [32]. The crack propagation behavior and changes in mechanical properties of sandstone under the influence of pore water pressure have also been investigated [33].

The current research has overlooked the correlation between rock mechanical properties and fracture development, as well as the influence of different physical fields on rock porosity and fractures. To address these issues, this study utilizes various experimental equipment to conduct tests on sandstone under different coupling conditions of stress, seepage, and temperature fields. Additionally, numerical simulation experiments on a random fracture model are performed to investigate changes in mechanical properties and fracture evolution characteristics. Permeability monitoring and numerical simulation methods are used to consider the influence of physical fields and primary fractures on the failure process of the sandstone samples. Based on this, a rock constitutive model that takes into account fracture development is established. These findings provide a theoretical foundation for actual deep mining projects.

2. Research methods

The rock samples for the test were collected from the sandstone located at a depth of 40 m in a mine in Zigong, Sichuan Province. The mining area primarily consists of a semi-hard rock formation, which is predominantly composed of sand and mudstone from the

Table 1
Sample IQ value.

Sample No	IQ value	Sample Name
01	86.37 %	D-1
02	84.10 %	D-2
1	85.60 %	25-30-0
2	84.85 %	25-40-5
3	85.40 %	75-40-10
4	86.63 %	75-30-5
5	87.17 %	75-40-5
6	87.42 %	75-50-5
7	86.51 %	75-40-0
8	88.04 %	125-40-5
9	87.04 %	125-50-10
10	85.58 %	100-40-5
11	86.00 %	75-40-20
12	92.46 %	/
13	93.37 %	/

Shaximiao Formation of the Jurassic system. Following the guidelines outlined in the "Code for Rock Testing in Water Conservancy and Hydropower Engineering," the rock was processed into standardized cylindrical samples with a diameter of 50 mm and height of 100 mm. From a batch of rock samples, uniform and similar-sized samples were chosen for testing, ensuring consistent apparent distribution and quality. Test samples with comparable degrees of fracture were selected. The Index of Quality (IQ) value represents a quantitative measure of rock fracture. The IQ value of each rock sample was measured using an ultrasonic tester and can be calculated using the following formula 1:

$$IQ(\%) = \frac{V}{V^*} \times 100\% \tag{1}$$

where V represents the ultrasonic wave velocity of the tested sample, and V* represents the standard wave velocity of the corresponding rock type [34].

The sample IQ value is shown in Table 1.

The main experimental instruments used in the test include.

1. ZYB-II vacuum pressure saturation device: This device is utilized to fully saturate the rock samples.
2. Rock 600-50 VHT rock high-temperature triaxial rheological test system (see Fig. 1): This system enables accurate control of the rock loading rate, as well as real-time recording of stress and strain deformation during the experiment.

The experimental system consists of four main systems, which are as follows.

1. Master control and parameter recording system: This system is responsible for controlling and recording various parameters during the experiment.
2. Sample triaxial pressure system: This system applies pressure on the rock sample in a triaxial configuration. The maximum confining pressure that can be applied is 100 MPa, and the maximum axial pressure is 800 MPa. The system has a control accuracy of ±0.01 MPa and a pressure sensor accuracy of 0.01 % FS.
3. Seepage system: This system allows for the control of water pressure during the experiment. The maximum water pressure that can be applied is 50 MPa.

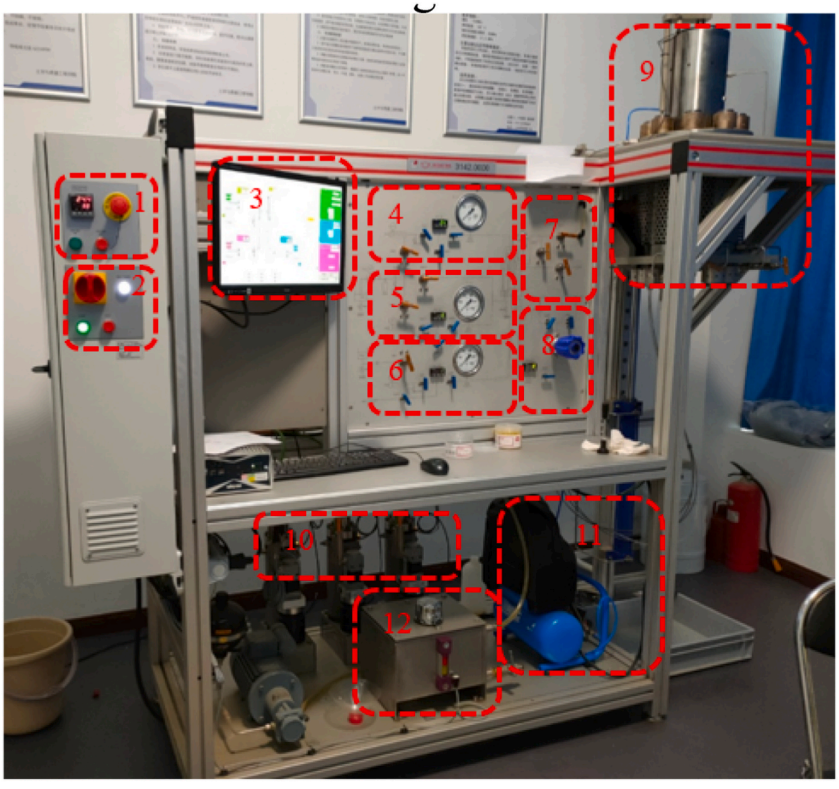

Fig. 1. Rock full stress multi-field coupling triaxial tester(1 - temperature control button 2 - main control switch 3 - computer display 4 - axial compression control system 5 - confining pressure control system 6 - inlet pore water pressure control system 7 - oil filling and drainage system 8 - outlet pore water pressure control system 9 - sample installation area 10 stress loading area 11 pressure pump 12 oil tank).

4. Temperature control system: The temperature control system includes an electric heating ring that heats the pressure chamber. Heat transfer is achieved through high-temperature and pressure-resistant oil inside the pressure chamber. The sample gradually heats up along with the temperature of the pressure chamber environment. The maximum temperature that can be reached is 200 °C, and the control accuracy is ±0.5 °C.

Sample packaging and sensor layout are shown in Fig. 2.

To ensure proper isolation of the sample from the external environment, a leather sleeve and a sealing ring are used. These prevent any contact between the sample and the oil used in the osmotic pressure system and the confining pressure loading system.

LVDT displacement sensors are installed on both sides of the sample to measure its axial strain. These sensors assist in accurately recording the deformation of the sample during the experiment.

To accommodate the axial deformation of the sample, the seepage outlet pipeline is equipped with a spring-like structure on the lower side. This structure allows for better flexibility in adjusting to changes in the spacing between the upper and lower parts of the sample.

In this experiment, the complex stress-seepage-temperature multi-field coupling in deep rock is simulated using a rock full-stress multi-field coupling triaxial apparatus. The table below (Table 2) provides information regarding the sample numbers and the corresponding test conditions to be tested.

Based on the experimental results, the obtained mechanical characteristic parameters are presented in Table 3.

3. Analysis of test results

3.1. Mechanical characteristics of sandstone under multi-field coupling

3.1.1. Sandstone strain behavior

By plotting the relationship between axial, transverse, volume strain, crack volume strain, and axial stress, the failure process of rock samples can be effectively studied. This analysis allows for the extraction of characteristic points related to the crack development stage in the fracture process. Fig. 3 illustrates the relationship between axial, transverse, volume strain, crack volume strain, and axial stress, as well as the change characteristic points of the stress-strain curve.

In Fig. 3, it can be seen that under the action of preload and pure hydrostatic confining pressure, the pores inside the sample have been compacted in advance, so the pore compaction stage is not obvious. Point O is the starting point of the curve; point A is the stress of the specimen. , the point where the strain begins to deviate from the linear growth position, and it is also the turning point of the crack strain of the specimen; point B is the turning point of the volume strain of the specimen; points D_1 and D_2 are determined based

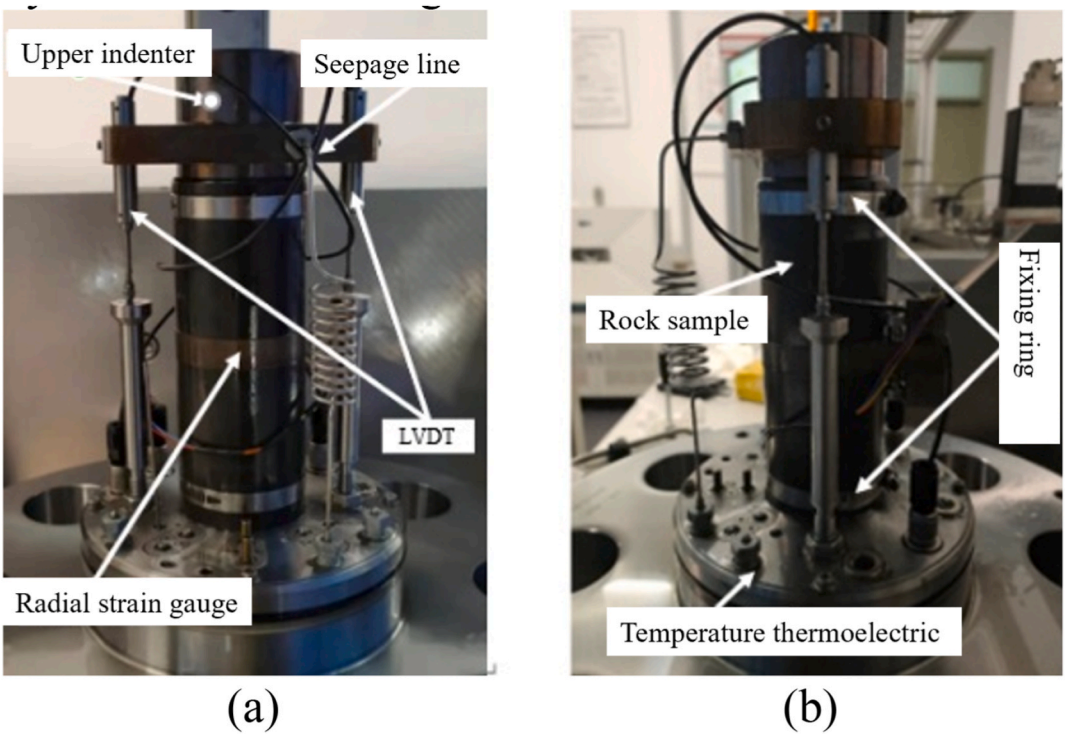

Fig. 2. Sample Package Diagram. (a) Front view (b) Side view.

Table 2
test conditions.

Sample No	Sample Name	Temperature/°C	Confining pressure/MPa	Osmotic pressure/MPa
01	D-1	25	0	0
02	D-2	25	0	0
1	25-30-0	25	30	0
2	25-40-5	25	40	5
3	75-40-10	75	40	10
4	75-30-5	75	30	5
5	75-40-5	75	40	5
6	75-50-5	75	50	5
7	75-40-0	75	40	0
8	125-40-5	125	40	5
9	125-50-10	125	50	10
10	100-40-5	100	40	5
11	75-40-20	75	40	20

(Note: No. 01 sample is not saturated).

Table 3
Mechanical properties of specimens.

Sample Name	Peak intensity (MPa)	Peak Axial strain	Peak radial strain	Elastic modulus (GPa)	Poisson's ratio
D-1	55.11	10.72	8.04531	4.45	0.20
D-2	36.77	7.12	4.01491	3.77	0.13
25-30-0	109.46	33.94	15.06185	5.58	0.26
25-40-5	120.35	32.38	7.98829	5.88	0.16
75-40-10	126.01	35.82	14.11052	5.51	0.18
75-30-5	112.29	28.65	11.39534	6.03	0.21
75-40-5	128.41	32.30	11.76554	6.31	0.19
75-50-5	152.89	36.48	11.69825	6.74	0.06
75-40-0	124.61	29.85	11.07772	7.08	0.20
125-40-5	130.86	32.75	12.51503	5.92	0.17
125-50-10	138.96	38.52	13.81273	6.41	0.14
100-40-5	132.63	31.37	11.70039	6.56	0.19
75-40-20	113.17	29.15	14.72379	5.20	0.25

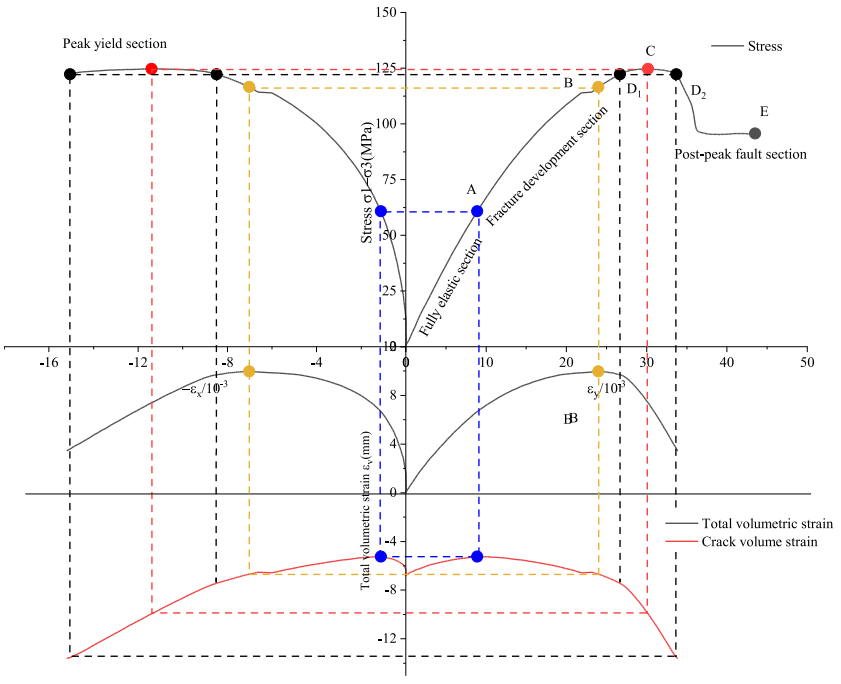

Fig. 3. The total stress-strain curve and mechanical characteristic points of 75-40-0 under multi-field coupling.

on the fact that the specimen stress does not change significantly but the strain continues to increase; C Point is the peak stress point; point E is the end point of the curve. The stress-strain curve divided by these points mainly presents four stages:

The first stage is the O-A section, which is fully elastic. In this stage, except for a very small amount of fracture pore deformation, the deformation of the sample is mainly elastic, and the overall curve is approximately a straight line.

The second stage is the A-D_1 section, which represents the propagation of cracks. With the increase in axial pressure and the transition of crack propagation specimen from elastic deformation to plastic deformation, the internal crack propagation speed accelerates. In this stage, the specimen under triaxial compression exhibits a peak yield plateau section, which is different from the uniaxial specimen. The effect of confining pressure causes the test to shift from brittle failure to ductile failure. At the same time, as cracks continue to develop, the volume strain of the sample changes direction and shows compression expansion.

The third stage is the D_1-D_2 section, which represents the peak yield. Under the influence of multi-physics field coupling and crack propagation, after the strength of the sample reaches a certain value, there is a creep-like stage where the stress remains unchanged while the strain continuously increases. This stage is called the peak yield section. During this stage, the radial strain and crack's volume strain of the sample increase rapidly, and the internal crack of the sample develops rapidly.

The fourth stage is the D_2-E section, which represents the residual strength. After the internal cracks of the sample rapidly develop to a certain extent at the peak yield stage, the sample experiences structural damage, causing a sharp drop in strength. However, even

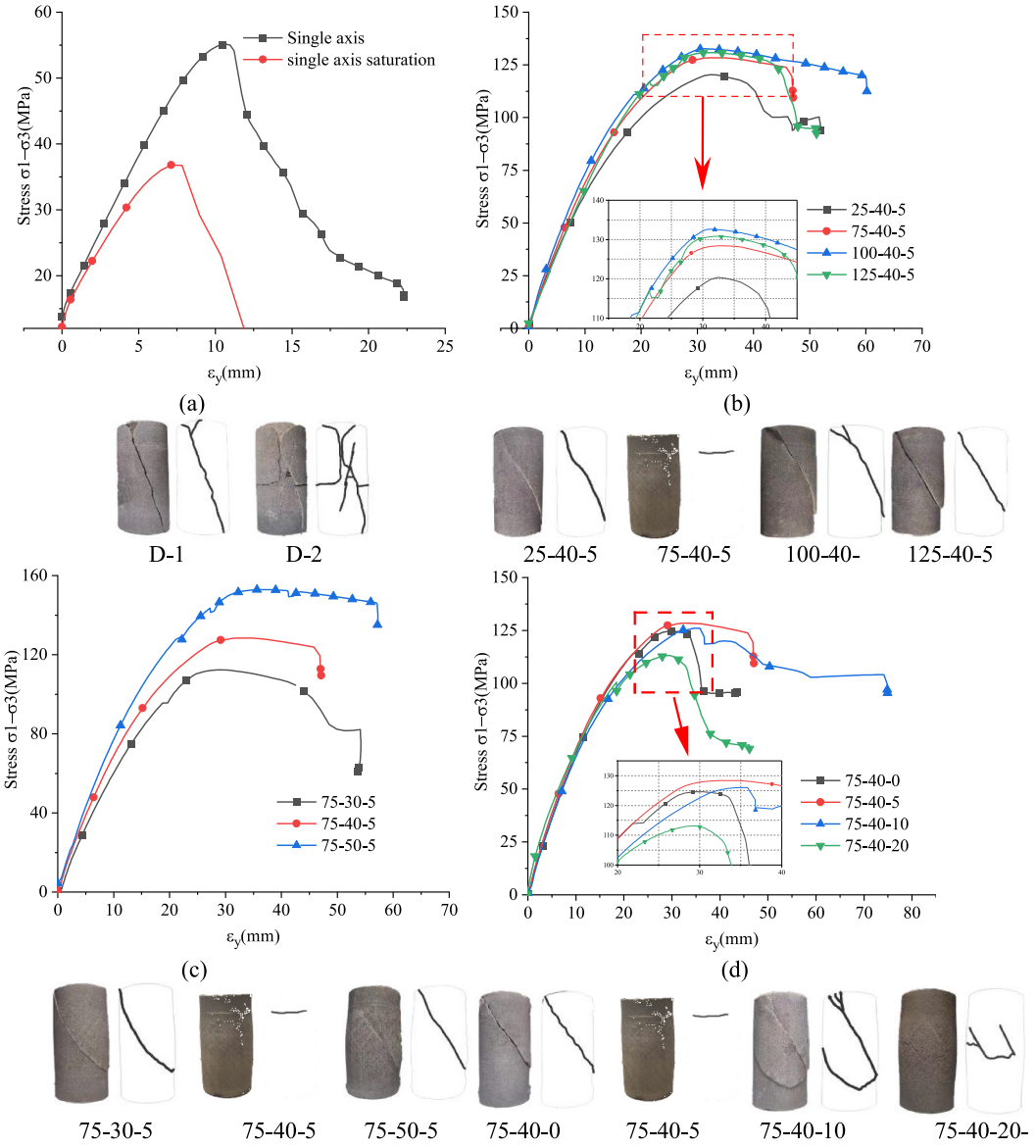

Fig. 4. Stress-strain and failure under different conditions:(a) Stress-strain curve under uniaxial compression; (b) Stress-strain curves at different temperatures; (c) Stress-strain curves under different confining pressures,and(d) Stress-strain curves under different osmotic pressures.

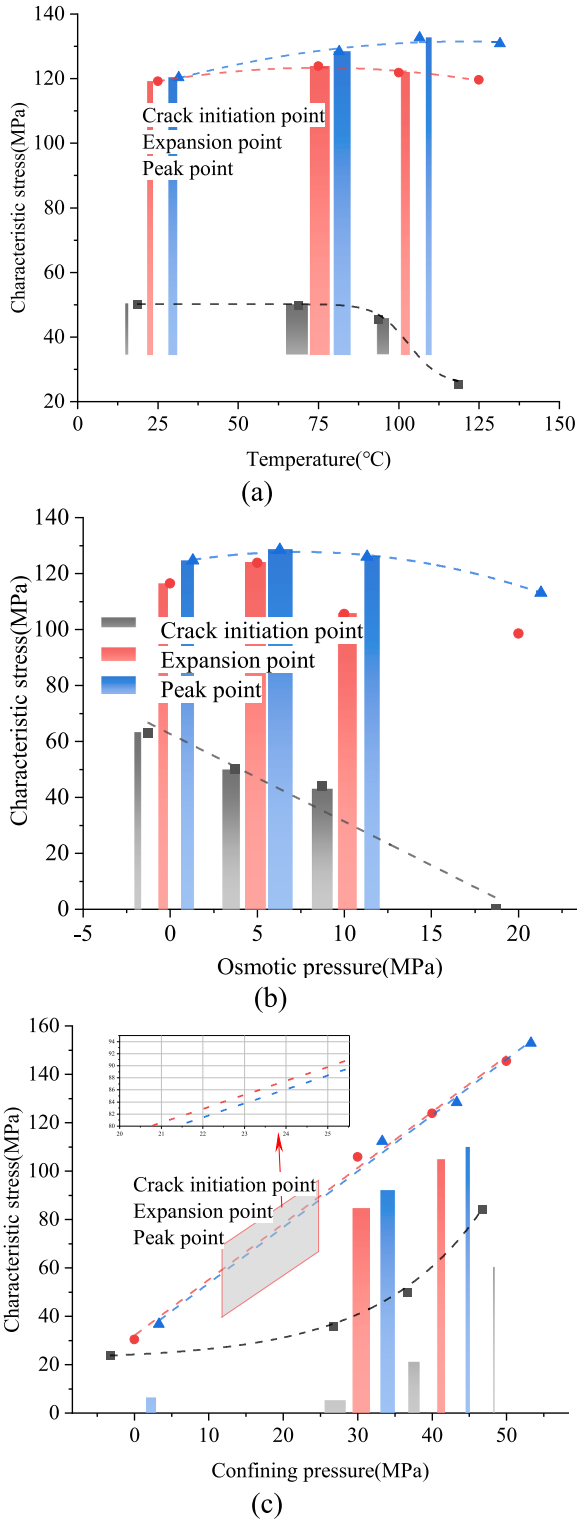

Fig. 5. Changing trend of the strength of characteristic points of samples under different physical fields:(a)Change the trend of characteristic points at different temperature; (b) Change the trend of characteristic points of different osmotic pressure, and (c) Change the trend of characteristic points of different confining pressure.

after reaching the peak, the triaxial compression specimen still retains some bearing capacity due to the confining pressure, resulting in a residual strength platform.

3.1.2. Stress-strain curve and failure mode of sandstone

Under the influence of different physical fields, Fig. 4 shows the stress-strain curve and fracture mode of the sample.

As demonstrated in Fig. 4 (a), the peak strength of the saturated sample in the uniaxial test is 33 % lower than that of the conventional sample. Furthermore, the failure mode shifts from tension-shear combined failure to structural plane shear failure. It should be noted that pore water significantly weakens the strength of the internal structural plane.

Fig. 4 (b) illustrates that the stress value and the peak yield section length of the stress-strain curve of the sample increase initially and then decrease with rising temperature under the same strain condition. Additionally, under triaxial compression, the mechanical strength of the sample at 100 °C is the highest, suggesting a turning point in the influence of temperature on the mechanical strength and failure resistance of the rock.

Analysis of the curve in Fig. 4 (c) reveals a trend of steady increase in the mechanical strength of rock samples with increasing confining pressure.

Observation of Fig. 4 (d) indicates that under a confining pressure of 40 MPa, osmotic pressure below 10 MPa does not significantly weaken the mechanical strength of the rock. In fact, the peak strength of the rock under 5 MPa osmotic pressure is even greater than that without osmotic pressure, and the yield platform is longer. However, the peak strength of the rock decreases significantly under the influence of 20 MPa osmotic pressure.

Observe the failure of the sample in Fig. 4. The failure mode of the saturated sample under the multi-field coupling action is a weak structural plane shear failure. Additionally, the failure surface of the sample under osmotic pressure is smoother compared to the sample without osmotic pressure. When the sample with an osmotic pressure of 10 MPa is damaged, the internal secondary structural plane weakens, resulting in the formation of two cracks. The full stress-strain curve of the 20 MPa osmotic pressure sample exhibits a peak, followed by the appearance of a residual strength platform section. However, no cracks are observed on the surface of the sample. The residual strength section of the 20 MPa osmotic pressure sample should be similar to that of the 10 MPa osmotic pressure sample. After the main structural plane under the osmotic pressure reaches the residual strength, the residual strength of the secondary structural plane is reduced again due to the high osmotic pressure.

3.1.3. Characteristic stress of sandstone

The stress-strain curve provides insights into the mechanical behavior of rock samples. In order to analyze the impact of different physical fields on various stages of sample failure, three characteristic points from Fig. 3 are extracted based on the phase characteristics of the stress-strain curve.

Crack initiation point A is defined as the point at which the sample's internal fracture begins to develop, marked by the turning point of the fracture volume strain [35].

Expansion point B is defined as the point at which the sample starts to expand, marked by the turning point of the total volume strain.

Peak point C is defined as the point at which the axial stress of the sample reaches its maximum during compression.

Fig. 5 illustrates the stress changes in different physical fields corresponding to crack initiation point A, expansion point B, and peak point C. It's evident from Fig. 5 that the changing trend of crack initiation strength, dilatancy strength, and peak strength of the sample under different physical fields is not the same:

In Fig. 5(a), it is observed that the peak stress and dilatancy stress undergo two stages of initial increase followed by a decrease as the temperature rises from 25 °C to 125 °C. This trend can be represented by a quadratic function. On the other hand, the crack initiation stress experiences three stages of gentle increase, followed by a decrease, and finally reaching a plateau, which is consistent with the Boltzmann fitting curve. It should be noted that the rock's crack initiation, dilatancy strength, and peak strength all decrease. The turning point of dilatancy stress occurs at a lower temperature than that of the peak stress. Under high confining pressure, the thermal expansion force of water is limited, causing the rock's fracture initiation strength to gradually level out instead of declining. However, due to the decrease in fracture initiation strength, internal fractures develop over time after the rock reaches the fracture initiation strength under pressure, leading to a continuous downward trend in rock dilatancy strength and peak strength.

In Fig. 5(b), as osmotic pressure increases, the dilatancy stress and peak stress of the sample initially increase and then decrease following an approximate quadratic function, while the crack initiation stress decreases linearly. This can be attributed to the generation of outward pressure in the internal pores and fractures of the sample when the osmotic pressure difference at both ends pushes seepage water through the sample, thereby accelerating fracture development. However, under lower water pressure (40 MPa confining pressure, 5 MPa seepage pressure), pore water can promptly fill new pore fissures, leading to a more uniform stress conduction in the rock and reducing stress concentration. As a result, the overall strength of the rock increases.

In Fig. 5(c)–a linear correlation is observed between the sample's dilatancy stress, peak stress, and confining pressure, while the fracture strength shows an accelerated increase. The expansion stress of the sample is nearly parallel to the change in peak stress. The confining pressure directly inhibits expansion in the rock fracture, and the increase in fracture strength is more significant than the increase in the overall strength of the rock.

3.2. Analysis of internal fracture propagation based on permeability change

The testing machine is capable of monitoring the osmotic pressure at both ends of the sample as well as the water content in the

water supply tank. Additionally, the transient method can be employed to measure the permeability of the rock. The calculation formula 2 for rock permeability under this method is:

$$K_i = \frac{\mu L \Delta Q_i}{A \Delta P \Delta t_i} \tag{2}$$

Where: K_i is the average permeability of sandstone in time (m^2); μ is the fluid viscosity coefficient (Pa·s), and the dynamic viscosity of water changes with temperature and osmotic pressure; Δt_i s the interval time between recording points (s); ΔQ_i is the amount of water penetrating through the sandstone sample in Δt_i (m^3); ΔP is the differential pressure (Pa) between upstream and downstream of rock sample seepage.

The change in permeability of the sample shows a clear correlation with each stage of compression failure, and it can be used to assess the evolution of cracks. The relationship between crack volume strain, permeability, and axial strain is depicted in Fig. 6. As shown in the figure, the permeability of the sample exhibits a clear correlation with the volume strain of the cracks. The change in permeability can be divided into four stages, which align with the four stages of the rock stress-strain curve mentioned earlier.:

The first stage, known as the fully elastic stage or pore water precipitation stage, occurs when the sample is under fully elastic conditions. At this stage, the internal stress within the sample is insufficient to induce crack formation. However, as the axial strain increases, the pores and cracks inside the sample are compressed, resulting in an increase in crack volume strain. The pressure causes the pore water inside the saturated sample to seep out, leading to a lowering of the permeability. This phenomenon reaches its lowest point.

In the second stage, called the crack expansion stage, the axial strain continues to increase. Once the crack initiation stress is reached, the volume strain of the cracks starts to decline, indicating the development of cracks within the sample. The permeability gradually increases, shifting from a low value to a higher value. This stage is characterized by simultaneous crack expansion and pore

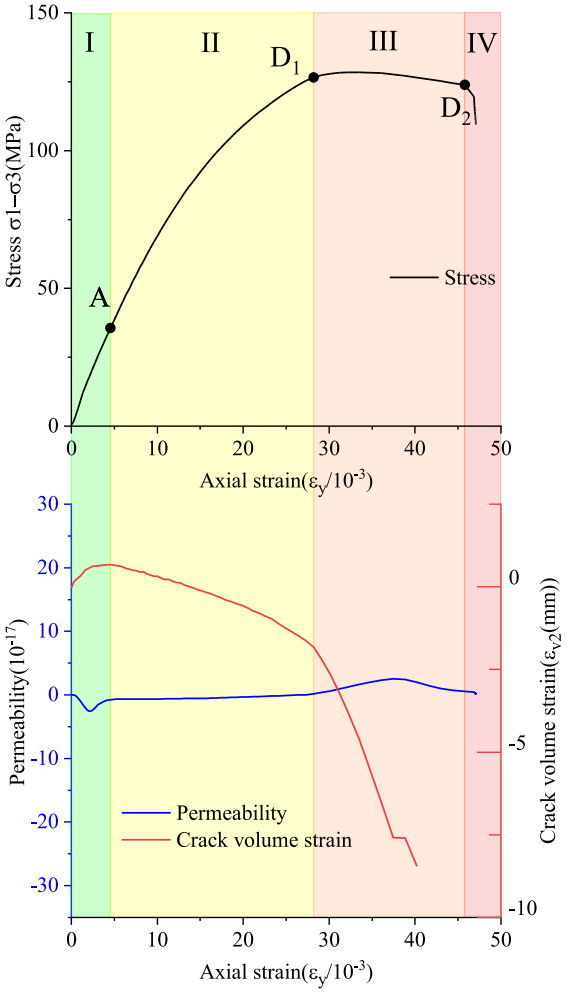

Fig. 6. Relationship between sample permeability and crack volume strain.

pressure increase. However, the effect of pore water precipitation still dominates, resulting in a permeability value higher than the predetermined value, but still negative.

The third stage occurs when the axial strain reaches a certain level. At this point, a significant number of pores and cracks are generated within the sample, causing a rapid decrease in crack volume strain. This leads to the infiltration of a large amount of seepage water into the sample, resulting in a sharp increase in permeability.

In the fourth and final stage, the internal pores and cracks of the sample are filled with water, causing the sample's cracks to continue expanding. This stage is characterized by a flat permeability curve, indicating that the permeability remains relatively constant. However, the permeability value is significantly higher than the initial value attained prior to the flat curve.

The changes in permeability are closely related to the development of pores and fractures within the sample, and the development of fractures can be inferred from the macro perspective by observing the changes in permeability. Fig. 7 illustrates the variations in internal permeability of the sample under different physical conditions. (a) Changes in permeability under different temperatures, (b) Changes in permeability under different osmotic pressures, (c) Changes in permeability under different confining pressures.

As the temperature increases, the internal pores and fractures of the sample expand due to heating. This expansion leads to a decrease in the amount of water released in the reverse direction under pressure, resulting in a decrease in the absolute value of the permeability valley observed in the first stage. Additionally, the different thermal expansion coefficients of water and sandstone contribute to a reduction in the seepage path generated by instantaneous rock failure along internal fractures under the combined effects of thermal expansion and seepage pressure. Consequently, the third stage advances, and the peak seepage pressure decreases. After the temperature reaches 125 °C, there is no distinct third stage observed.

Under a confining pressure of 40 MPa and 75 °C, compared to an osmotic pressure of 5 MPa, the precipitation of pore water is reduced under osmotic pressures of 10 MPa and 20 MPa. This reduction leads to a significant decrease in the valley value observed in the first stage of the permeability change curve. An increase in pore water pressure promotes the penetration and expansion of rock fractures, resulting in the gradual advancement of the peak value observed in the third stage. Furthermore, the permeability change curve shows a second increase in permeability during the fourth stage. This secondary development of internal pore cracks corresponds

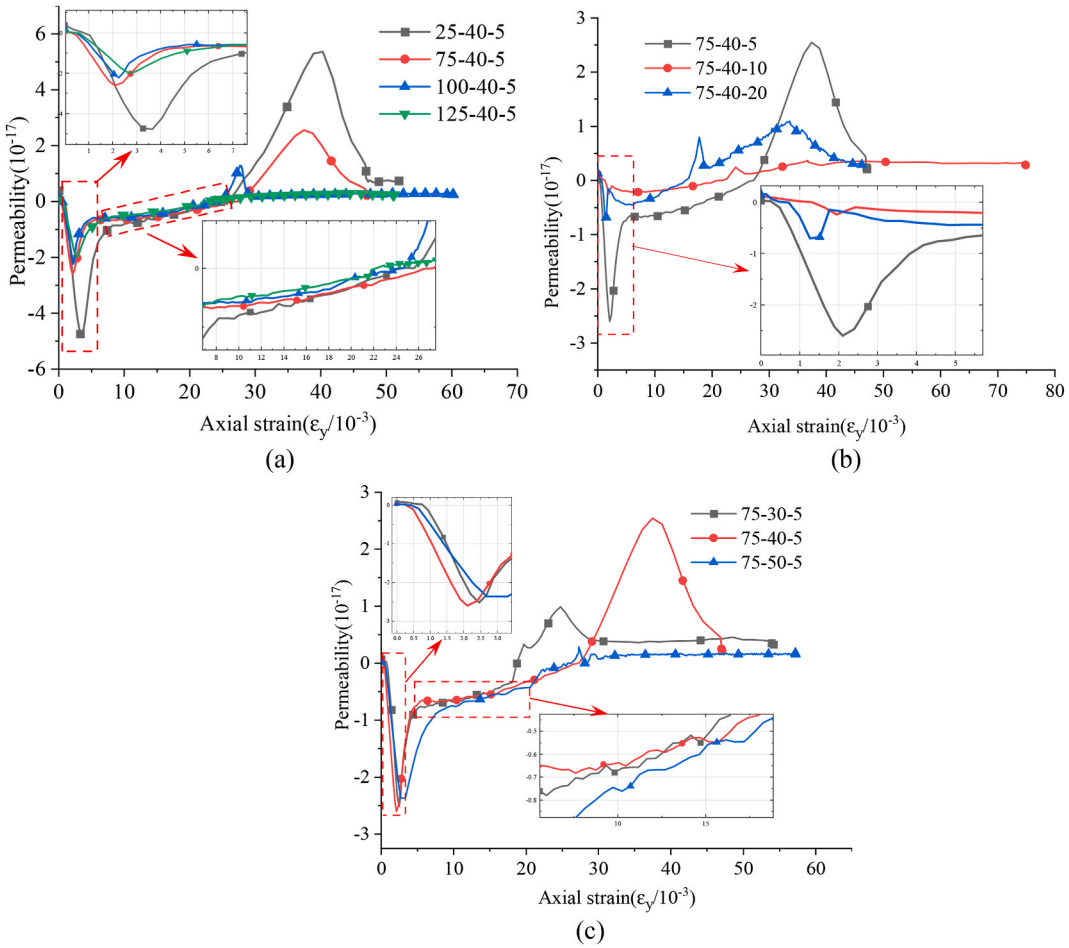

Fig. 7. Change of sample permeability under different physical fields: (a) Permeability change at different temperatures:(b) Permeability change under different osmotic pressures, and(c) Permeability change under different confining pressures.

to the appearance of secondary cracks on the sample's surface, as depicted in Fig. 4. It further indicates damage to the secondary structural plane of the sample under the influence of 10 MPa and 20 MPa osmotic pressure.

With an increase in confining pressure, particularly during the loading process of pure hydrostatic pressure, the pore water in the sandstone sample is less affected, resulting in minimal changes in the valley value observed in the first stage. However, when the sample undergoes damage under pressure, the internal pore cracks diminish, causing the gradual reduction and disappearance of the peak value observed in the third stage. Ultimately, the permeability of the rock sample in the fourth stage also decreases gradually.

3.3. Multi-field coupled rock numerical simulation considering primary fractures

Nuclear magnetic resonance equipment measures the internal porosity and pore size distribution of rocks. The internal pore size distribution of the rock sample (Fig. 8).

Use COMSOL software and random fracture modeling method [36] to establish a two-dimensional random fracture model, which is convenient for studying the development and expansion of fractures in the sample affected by multi-field coupling. This random model building method determines the size, shape, porosity and crack size range of the model, and uses a random algorithm to create multiple cracks with different angles, positions, and sizes. When the porosity is close to the set value, it stops generating cracks and calculates The true porosity completes the establishment of the entire model.

The numerical model of the sample is built with COMSOL software and based on the pore data of nuclear magnetic resonance. The model size is consistent with the central longitudinal section size of the sample, which is 100 mm long and 50 mm high. The model includes a rock module and a fracture module. The steps for establishing a numerical model with random cracks under the action of multiple physical fields include the following.

1 The random fracture model establishment code is compiled with MATLAB software, and the fracture size and distribution are macroscopically controlled according to the test data. At the same time, to make the phenomenon more obvious, the pore and fissure size in the model is enlarged compared with the actual rock pore and fissure size. The numerical simulation model with cracks is established, as shown in Fig. 9 below.
2 The couple and link COMSOL and MATLAB software to import the random fracture model into COMSOL.
3 The calculation model parameter's setting conditions are to better fit the saturated sandstone samples used in the test. Two different materials are used in the model pore's interior and the model's pore main body, and different physical and mechanical characteristics parameters are given. See Table 4 for rock material parameters and test conditions. Pore water material parameters are based on COMSOL conventional water material.

By numerically simulating the crack model, you can directly observe the entire process of crack evolution in the specimen. Obtain information about crack development and stress distribution at the crack initiation and peak positions in the specimen under the influence of stress-seepage coupling. Refer to Table 5 and Table 6 for these results. In the tables, the red arrow indicates the direction of the maximum principal stress at the stress concentration position, and its magnitude represents the magnitude of the principal stress.

According to Table 5, during the compression process of the specimen, stress concentration regions of X type appear at the tip of each crack. As the confining pressure increases, the crack with the highest stress concentration moves from both ends of the sample towards the middle. Additionally, the direction of the principal stress gradually changes from being perpendicular to the crack to parallel to the crack. Moreover, the mode of fracture propagation shifts from failure along the crack trend to failure through multi-fracture connection.

As the lower osmotic pressure continues to strengthen, the direction of the principal stress gradually changes from parallel to the crack to being perpendicular to the crack. Simultaneously, the mode of crack expansion changes from failure through multi-fracture connection to failure along the crack trend. The crack with the highest stress concentration moves from the middle of the specimen to the upper end.

In summary, except for the position of stress concentration, osmotic pressure and confining pressure have opposite effects on the internal cracks of the specimen.

Table 6 presents a comprehensive view of sample failure cracks. The final failure of the specimen is strongly influenced by the crack initiation, and the ultimate failure mode is characterized by shear failure along the structural plane in the direction of the crack. Similar to the observations in Table 5, as the confining pressure increases, the final failure mode of the specimen transitions from shear failure

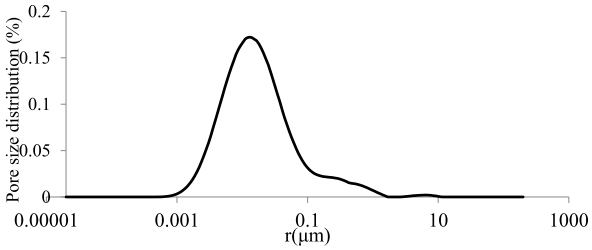

Fig. 8. Pore size distribution.

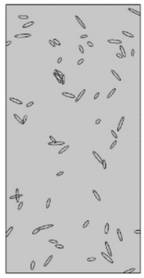

Fig. 9. Random fracture model of rock.

Table 4
Rock material simulation parameters.

Parameter name	Symbol	Unit	Value
Temperature	T	K	298.15/348.15/373.15/398.15
Osmotic pressure difference	Π	MPa	0/5/10/20
Confining pressure	*Pc*	MPa	30/40/50
Thermal conductivity	λ	W/(m·K)	2.34
Constant pressure heat capacity	Cp	J/(kg·K)	970
Model density	*ρ*	Kg/m3	2537
Young's modulus	E	GPa	6.3
Poisson's ratio	*υ*	1	0.24
Cohesive force	c	MPa	9.932
Internal friction angle	*φ*	°	33.25
Coefficient of thermal expansion	α	1/K	1e-5

along the crack direction to tensile failure between cracks. This trend is particularly pronounced in simulated specimens without osmotic pressure, such as the 25-40-0 and 25-50-0 specimens.

As the osmotic pressure increases, the occurrence of tensile failure in the sample decreases. The failure position gradually shifts to a higher level above the model.

Therefore, the development of confining pressure and osmotic pressure have opposite effects on the final failure mode and position of cracks within the specimen.

4. Rock strength constitutive model considering fracture development

Previous researchers and scholars have found that internal cracks in rocks play a crucial role in the gradual failure process of rocks [37]. In the analysis of the characteristic points of the 3.2 sample, it is found that the variation trend of rock initiation stress and peak stress is different. Thus, the rock sample can be divided into intact rock microelements and fractured microelements for property analysis. At the same time, there is a significant correlation between the development stage of internal cracks and the stress-strain curve, as observed in the permeability analysis in section 3.3. Furthermore, numerical simulations in section 3.4 reveal that different physical fields have varied effects on internal cracks, which ultimately impact the overall strength and failure characteristics.

To better describe the constitutive relation between strength reduction and failure caused by the gradual development of cracks in the rock compression process, as well as the influence of different physical fields on internal fractures, a rock mechanics constitutive model with cracks is constructed. The following four hypotheses are proposed.

Hypothesis 1. Rock can be regarded as composed of fractured microelement and intact rock microelement, both of which affect the rock strength.

Hypothesis 2. The stress required for the expansion of the main fracture in the rock remains unchanged, which is referred to as the crack initiation stress of the rock.

Hypothesis 3. Prior to reaching the initiation stress, the rock fractures do not expand significantly, and the influence of the rock fracture compaction stage is minimal.

Hypothesis 4. The complete rock microelement is considered as a Maxwell's body.

The constitutive equation is established as follows, which is divided into two segments; the first segment is before reaching the crack initiation stress of the rock, this part adopts the Maxwell body model according to the previous hypothesis, and the second is the introduction of the fracture body segment.

Table 5
Development characteristics of crack initiation stress cracks.

Characteristic stress interval	Characteristics of fracture development			
Crack initiation stress interval	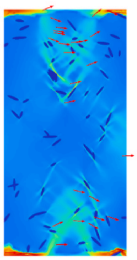 25-30-0	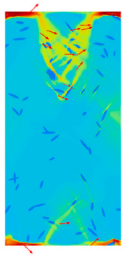 25-30-5	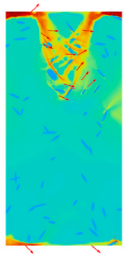 25-30-10	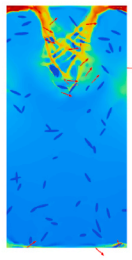 25-30-20
	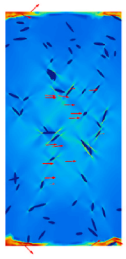 25-40-0	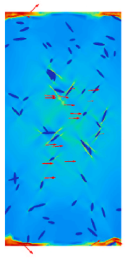 25-40-5	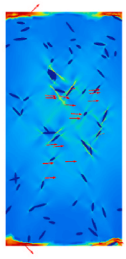 25-40-10	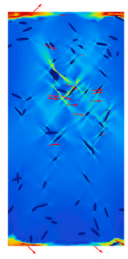 25-40-20
	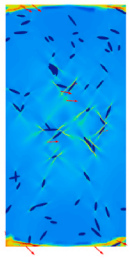 25-50-0	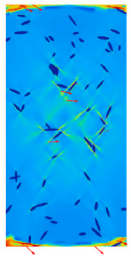 25-50-5	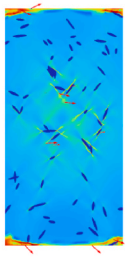 25-50-10	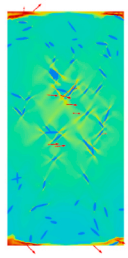 25-50-20

$$\sigma_f = \begin{cases} E_c \cdot \left(\varepsilon - \dfrac{T \cdot \sigma}{\eta}\right) & (\sigma \le F_c) \\ E_c \cdot \left(\varepsilon - \dfrac{T \cdot \sigma}{\eta}\right) \cdot (1-n) + n \cdot F_c & (\sigma > F_c) \end{cases} \tag{3}$$

Where E_c is the elastic modulus of intact rock, n is the variable of rock initiation degree, T is compression time, Fc is rock initiation stress, ε is rock strain and η is viscosity coefficient.

The variable n, representing the rock crack initiation degree, is dependent on the stress and time of the rock. As depicted in Fig. 10, the variation trend of the n value and stress follows a close positive S shape, which is in accordance with the Boltzmann regression equation. The fitting curve has an R^2 value of 0.98646, indicating a good fit and a strong correlation.

After further data analysis and fitting, the expression for the n value can be obtained as follows:

$$n = \sigma \cdot \left(A_2 + \frac{A_1 - A_2}{1 + e^{\frac{T_1 - T_0}{dT}}}\right) \tag{4}$$

Where is the deviatoric stress, the T1 is the compression time after the specimen reaches the initiation stress, and the A1,A2,T0, dT is the correlation coefficient of the fitting curve.

The Boltzmann regression equation, which describes the statistical behavior of a thermodynamic system in a non-equilibrium state, can be applied to describe the variation of macroscopic quantities in a thermodynamic system. In the context of Griffith's fracture theory, cracks are the result of stress concentration caused by microcracks in a material. According to energy balance principles, crack propagation occurs due to the release of stored elastic strain energy during deformation. Therefore, the propagation of rock cracks can

Table 6
Development characteristics of peak stress cracks.

Characteristic stress interval	Characteristics of fracture development			
Peak stress range	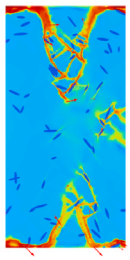 25-30-0	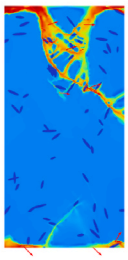 25-30-5	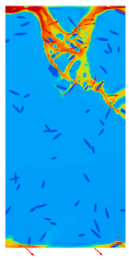 25-30-10	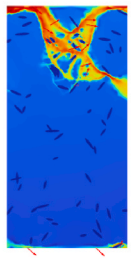 25-30-20
	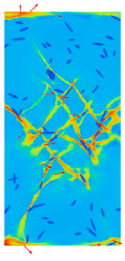 25-40-0	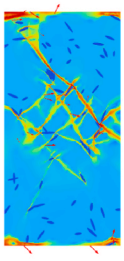 25-40-5	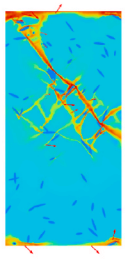 25-40-10	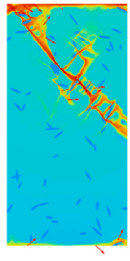 25-40-20
	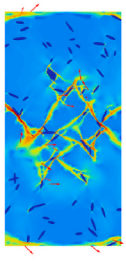 25-50-0	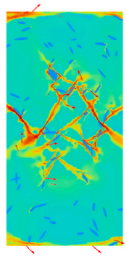 25-50-5	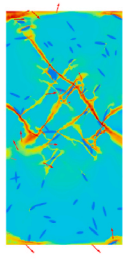 25-50-10	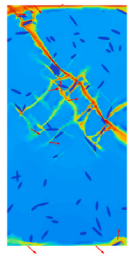 25-50-20

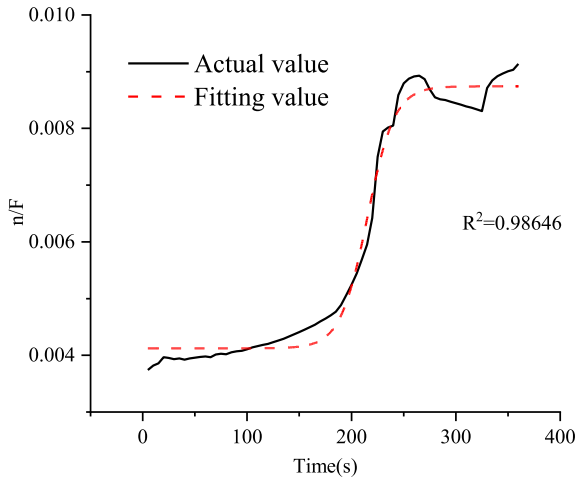

Fig. 10. Fitting curve of rock cracking degree.

be understood as a thermodynamic energy dissipation problem. It is scientifically and logically appropriate to fit the n value of rock fracture development using the kinetic Boltzmann regression equation, as it describes the energy change in a thermodynamic system.

The constitutive model, obtained by piecewise fitting of equation (3), is compared with the original stress-strain curve in several cases, as shown in Fig. 11. (a) (b) (c) (d) in Fig. 11 are comparisons of test results and simulation results under different physical field conditions. It can be observed that the fitting curve has an R2 value greater than 0.97, indicating a good fit. The fitting curve adequately reflects the gradual yielding of rocks in the compression process, as evidenced by the comparison.

5. Discussion

5.1. The influence of multi-field coupling on internal cracks

The thermal damage to rock micro-crystal structures primarily occurs at temperatures above 200 °C [29]. Therefore, in the third chapter, the change in mechanical properties of rocks under the influence of temperature is predominantly due to the thermal expansion of the rock itself and internal pore water. The effect of temperature on the fracture model is illustrated in Fig. 12. Fig. 12 (a), (b), (c), and (d) show the stress distribution of internal pores affected by thermal expansion at 25 °C, 75 °C, 100 °C, and 125 °C respectively.

It is evident that at lower temperatures, both the rock and pore water expand with increasing temperature. This leads to a more uniform stress distribution within the rock when it is compressed, reducing stress concentration and enhancing the overall strength of the rock. As the thermal expansion effect of water is relatively small at low temperatures, the micro-fracture structure is minimally affected by the pressure of internal pore water expansion, and the fracture strength of the rock is not significantly influenced. However, as the temperature continues to rise, the differential thermal expansion between the rock and water becomes more pronounced. This results in a stronger thermal expansion effect of the pore water, causing tensile stresses to be exerted on the internal pores and facilitating crack propagation. In general, an increase in temperature leads to higher tensile stresses at the crack tip and amplifies the

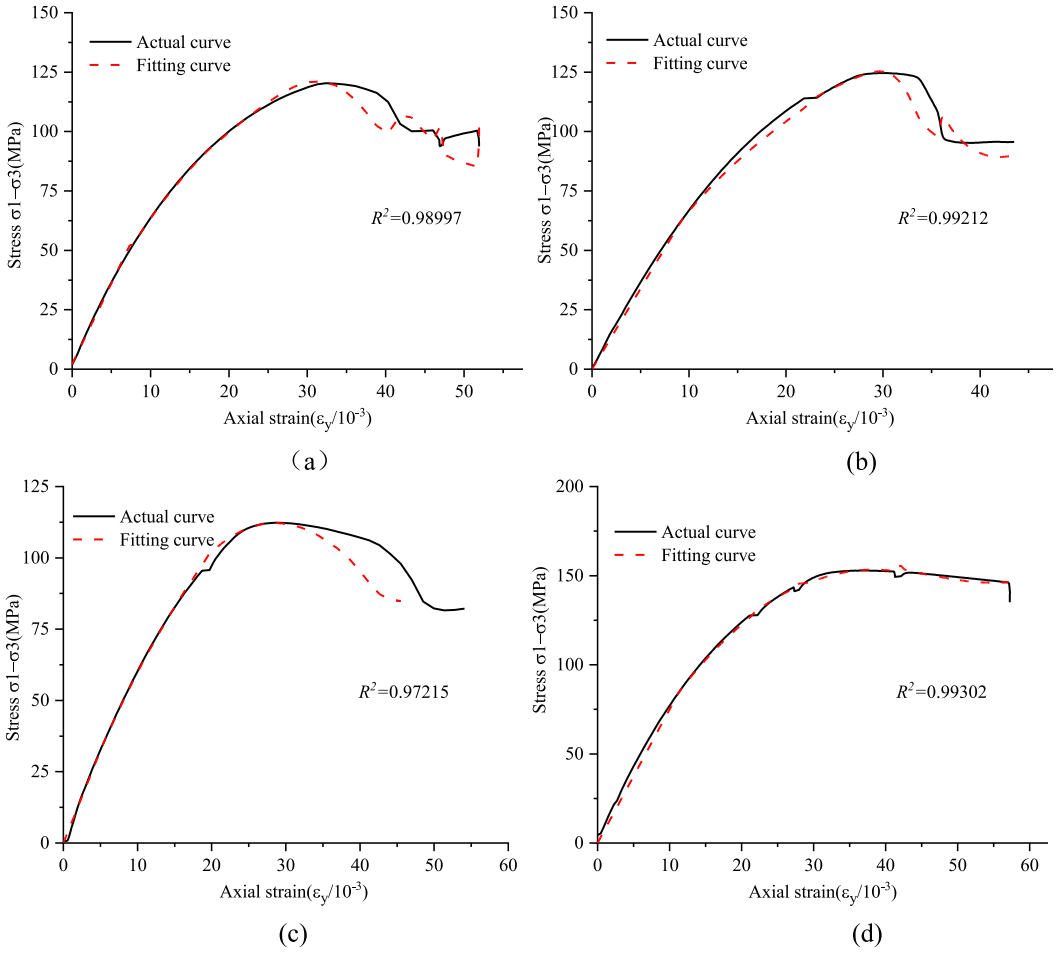

Fig. 11. Fitting curve of the constitutive model of fracture body: (a) 25-40-5 fitting curve; (b) 75-40-0 fitting curve; (c) 75-30-5 fitting curve,and(d) 75-50-5 fitting curve.

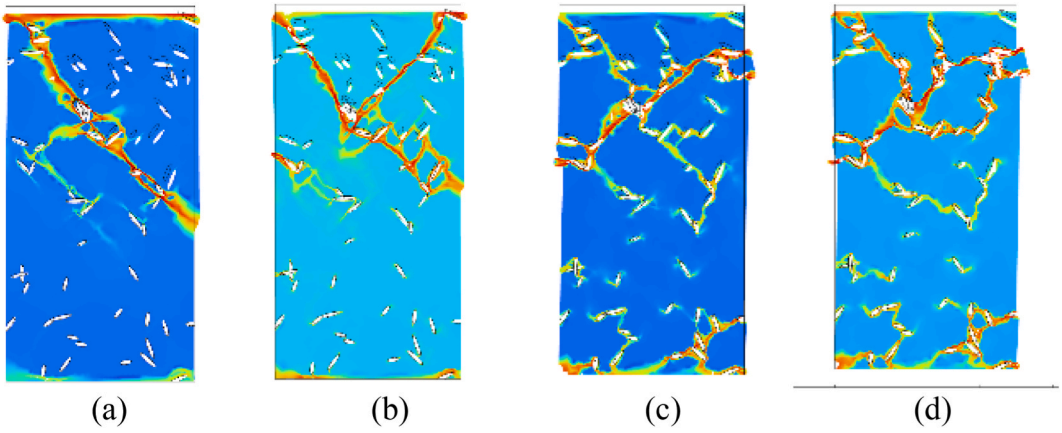

Fig. 12. The damage of the crack model under the action of temperature:(a) 25 °C; (b) 75 °C; (c) 100 °C, and(d) 125 °C.

influence of pore fissures on the mechanical properties of the rock.

In the numerical simulation conducted in Chapter 4, it is observed that as the osmotic pressure increases, the shear plane of specimen failure gradually shifts up the model. This aligns with the rock failure mode observed in the laboratory test conducted in Chapter 3. By varying the osmotic pressure on the high-pressure side of the model, different failure modes on the high-pressure side can be obtained, as depicted in Fig. 13. In Fig. 13, the high-pressure side of the osmotic pressure of model (a) is above the model, and the high-pressure side of osmotic pressure of model (b) is below the model.

By examining Fig. 13 along with the model failure modes presented in tables 5 and 6 and it can be determined that the low-pressure

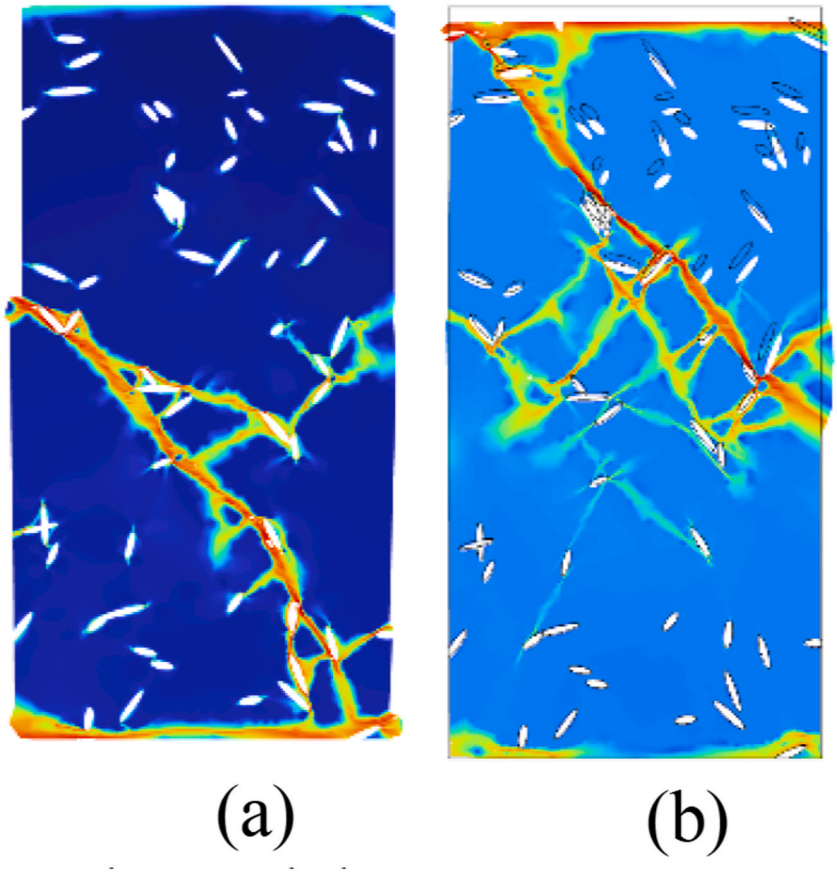

Fig. 13. Failure mode of fracture mode model under different seepage pressures:(a) The upper osmotic pressure high-pressure side; (b) the Lower osmotic high-pressure side.

side of the osmotic pressure on the sample is more susceptible to failure. Conversely, the presence of osmotic pressure provides a certain level of protection against failure on the high-pressure side.

Based on the above discussion, the changes in mechanical properties and failure mode of rock under the influence of the temperature-seepage-stress physical field are mainly due to the impact of the physical field on its internal pores and cracks. Generally speaking, the temperature field and seepage field enhance the influence of pore fractures on the overall strength of the rock, while the confining pressure weakens the impact of pore cracks.

Additionally, the effect of temperature increase on pore fractures is related to their size. The larger the size of the pore fracture, the more significant the effect. Seepage also exhibits clear directionality, with pore fractures on the side of osmotic pressure being more prone to expansion. The effect of confining pressure on rock pore fractures is dependent on the magnitude of the pressure itself. Therefore, in the multi-field coupling environment of deep engineering, the failure of various mining exposed surfaces as the osmotic pressure side needs to be thoroughly analyzed in conjunction with surface and internal pore fissures.

In subsequent research, it is necessary to further apply new experimental equipment and technologies. In-situ CT equipment should be utilized to observe the microscopic changes in temperature and seepage fields within water-filled pores and cracks inside the sample. Acoustic emission positioning equipment should also be used to determine the location and timing of sample rupture, in order to further elucidate the mechanisms underlying changes in rock properties under the influence of deep geothermal conditions.

5.2. Characteristics of correlation coefficient of the constitutive model

Based on the fitting equation (4) and the quotient fitting image of the n-value and stress, the changing trend of the coefficients A1, A2, T0, and dT under different conditions can be calculated. These calculations are illustrated in Fig. 14. (a), (b), (c), and (d) in Fig. 14 respectively represent the changes in the four characteristic coefficients A1, A2, T0, and dT under different temperatures, osmotic pressure, confining pressure, and crack initiation stress.

As depicted in the figure, several observations can be made. Firstly, as the temperature increases, both A1 and A2 decrease, while T0 fluctuates without significant changes, and dT initially increases and then decreases with no noticeable change. Secondly, as the osmotic pressure increases, A1 decreases, A2 initially decreases and then increases, T0 fluctuation decreases, and dT fluctuation remains stable. Thirdly, with the increase in confining pressure, A1 initially increases and then stabilizes, A2 decreases initially and then stabilizes, and both T0 and dT initially stabilize and then increase with the rise in confining pressure. Finally, with the increase in crack initiation stress, A1 and A2 fluctuate without a clear correlation, while T0 and dT first stabilize and then increase.

Through equation (4), it is evident that A1 and A2 have an impact on the minimum and maximum values of the n-value, while T0 and dT influence the rate of change of the n-value. A larger T0 and dT correspond to a slower rate of change of the n-value over time. Thus, the greater the difference between A1 and A2 and the smaller the dT and T0, the more the constitutive relationship of the specimen is influenced by crack development. The difference between A1 and A2 varies depending on different conditions, as shown in Fig. 15. In Fig. 15, (a), (b), (c) and (d) respectively show the changing rules of A2-A1 with different temperatures, osmotic pressure, confining pressure and crack initiation stress.

Based on the analysis and diagram above, it can be observed that the constitutive relationship of the specimen initially decreases and then increases with an increase in temperature, and increases with an increase in osmotic pressure at a confining pressure of 40 MPa.

A1 reflects the initial degree of fracture failure within the specimen, with a smaller A1 indicating a higher initial fracture failure degree. On the other hand, A2 reflects the final fracture failure degree, with a smaller A2 suggesting a lower final fracture failure degree. The difference between A1 and A2 reflects the fracture failure degree of the specimen throughout the entire compression process. A smaller difference indicates that the mechanical properties of the specimen are less affected by the development of internal cracks.

Furthermore, T0 and dT reflect the extent to which the mechanical properties of the samples are influenced by the development time of internal cracks. A smaller T0 and dT indicate a greater influence of the development time of internal cracks on the mechanical properties of the samples.

This constitutive model effectively incorporates thermodynamics to depict the process of crack expansion and the time-dependent effects on the sample. It will be further validated through additional rock mechanics tests and analyzed using mesoscopic and microscopic testing methods. This will help establish the universality of the model and delve into the microscopic significance of its parameters.

6. Conclusions

In this study, in order to further understand the mechanical properties and failure conditions of rocks under different physical fields, conducted triaxial compression tests on sandstone specimens under various physical conditions using a rock full stress multi-field coupling triaxial tester. It investigated the effects of temperature, seepage and stress on the mechanical properties and failure modes of rocks. Based on the characteristic stress points in the compression process, it discussed the mechanism and law of how different physical fields influence the expansion of primary fractures in rock samples. It also observed the internal fracture propagation characteristics by establishing a random fracture numerical model. It proposed a rock constitutive model based on crack propagation. The main conclusions are as follows.

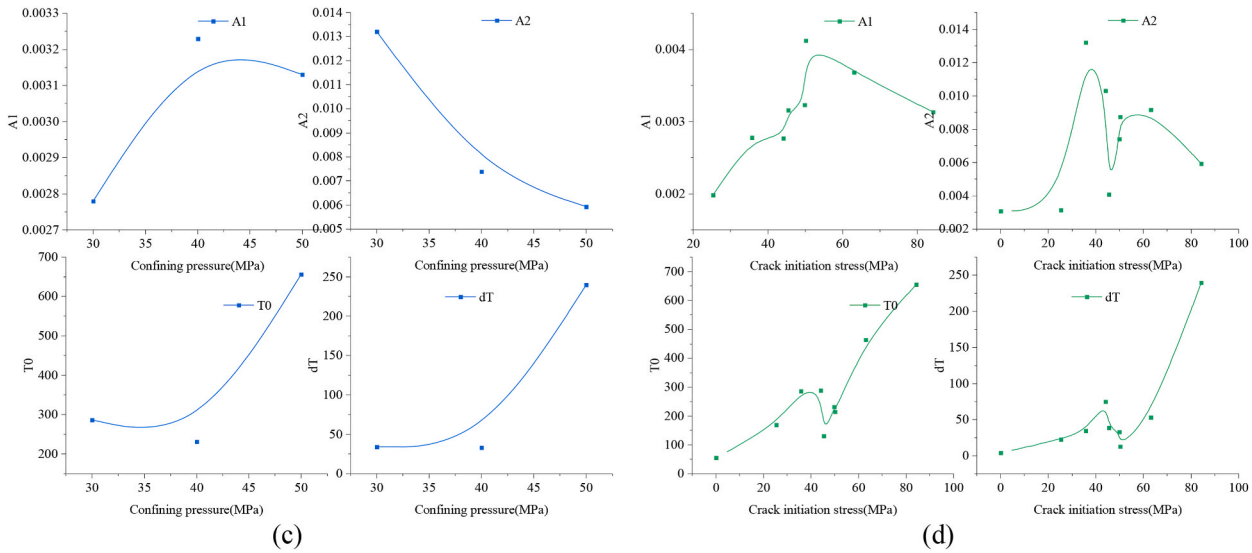

Fig. 14. Change trend of characteristic parameters of the constitutive model:(a) characteristic coefficients at different temperatures; (b) characteristic coefficients at different osmotic pressures:(c) characteristic coefficients at different confining pressures,and(d) characteristic coefficients at different initiation stress.

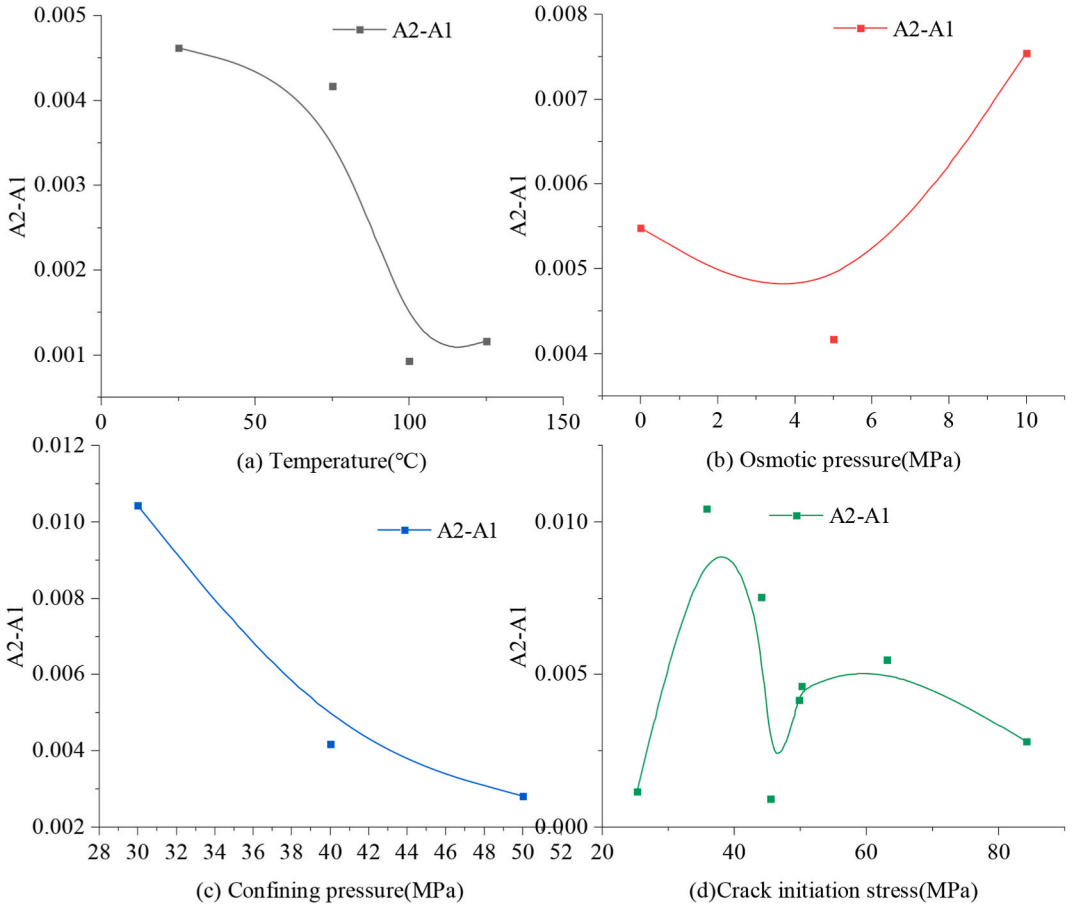

Fig. 15. Variation trend of difference between A_1 and A_2. (a) Temperature(°C) (b) Osmotic pressure(MPa) (c) Confining pressure(MPa) (d)Crack initiation stress(MPa).

(1) Under low ground temperature conditions, the slight thermal expansion effect can reduce the stress concentration during rock failure, thereby improving the rock strength; but when the ground temperature continues to rise, further enhancement of thermal expansion will produce tension on the pores, promoting pores and cracks development, reducing the overall strength of the rock.
(2) Based on the effect of 30–50 MPa confining pressure on rock samples, it can be inferred that the stress effect between deep surrounding rocks can effectively inhibit the expansion and development of internal pores and cracks, thereby improving the overall strength of the rock. This effect acts uniformly on inside the rock, and increases linearly with confining pressure.
(3) The permeability field often acts on rocks through the fluid medium in rock pores and cracks. Experimental results show that the low-pressure side of osmotic pressure is often more susceptible to damage. The seepage pressure difference causes pore water pressure to form in the rock and promotes pore development. The effect of osmotic pressure is affected by confining pressure. Under the confining pressure of 40 MPa, the effect is not obvious if the osmotic pressure is less than 10 MPa. Due to its similar effect to the temperature field, 5 MPa osmotic pressure can improve the mechanical strength of rocks.
(4) The influence of different physical fields on rock pores and microcrack structures is the main factor leading to changes in rock mechanical strength and macroscopic failure modes. Based on the relationship between rock failure and the influence of physical fields on the physical and mechanical properties of rock and its internal pores and cracks, a rock mechanics constitutive model that adds a rock crack development module is proposed. This constitutive model can better reflect the changes in stress and strain during rock compression under different physical conditions(R^2 is greater than 0.97). The equation coefficients reflect the development characteristics of rock cracks and the influence of physical fields, which has certain reference and application value.

Data Availability Statement

Some or all data, models, or code that support the findings of this study are available from the corresponding author upon reasonable request.

CRediT authorship contribution statement

Tianyi Shi: Writing – review & editing, Writing – original draft, Visualization, Validation, Software, Methodology, Investigation, Funding acquisition, Formal analysis, Data curation. **Jianxin Fu:** Writing – review & editing, Validation, Supervision, Software, Resources, Project administration, Funding acquisition, Conceptualization. **Weidong Song:** Validation, Resources, Funding acquisition. **Jie Wang:** Writing – review & editing, Supervision, Methodology. **Kazimi M. Y:** Writing – review & editing, Validation.

Declaration of competing interest

The authors declare that they have no known competing financial interests or personal relationships that could have appeared to influence the work reported in this paper.

Acknowledgements

This experimental work was financially supported by the National Key Research and Development Program of China (2022YFC2905003), the National Natural Science Foundation of China (Grant No. 52274109). Central University Basic Scientific Research Business Expenses Special Funds(Grant No. FRF-BD-20-03A).

References

[1] X. Wu, P. Li, Q. Guo, M. Cai, F. Ren, J. Zhang, Research progress in the evolution mechanism of physical and mechanical properties of thermally damaged rocks, Chinese Journal of Engineering Science 44 (2022) 827–839, https://doi.org/10.13374/j.issn2095-9389.2020.12.23.007.
[2] L. Yuan, Research progress of deep mining response and disaster prevention and control, Journal of Chinese Coal Society 46 (2021) 716–725, https://doi.org/10.13225/j.cnki.jccs.YT21.0158.
[3] L. Xie, X. Liu, X. Liu, Multi-field coupling law analysis of deep roadway based on lateral pressure difference. J. Saf. Environ.. (n.d.) 1–8. https://doi.org/10.13637/j.issn.1009-6094.2021.1787.
[4] Q. Zhang, J. Liu, Y. Zeng, Y. Liao, D. Xu, A. Zhu, Experimental study on permeability of gypsum rock under the condition of temperature-stress coupling, Chin. J. Rock Mech. Eng. 38 (2019) 1819–1827, https://doi.org/10.13722/j.cnki.jrme.2019.0162.
[5] G. Rong, J. Peng, M. Yao, Q. Jiang, L.N.Y. Wong, Effects of specimen size and thermal-damage on physical and mechanical behavior of a fine-grained marble, Eng. Geol. 232 (2018) 46–55, https://doi.org/10.1016/j.enggeo.2017.11.011.
[6] L. Xin, W. Cheng, J. Xie, Z. Liu, X. Hu, Numerical simulation study on the thermal-solid coupling of unidirectional heating of rocks, Coal science and technology, Coal science and technology 46 (2018) 145–151, https://doi.org/10.13199/j.cnki.cst.2018.07.023.
[7] C. Yao, Y. Shao, J. Yang, F. Huang, C. He, Q. Jiang, C. Zhou, Effects of non-Darcy flow on heat-flow coupling process in complex fractured rock masses, J. Nat. Gas Sci. Eng. 83 (2020) 103536, https://doi.org/10.1016/j.jngse.2020.103536.
[8] K. Huang, J. Xiong, Y. Yuan, Effect of different cooling methods on mechanical and acoustic characteristics of thermally damaged sandstone, Petrochemical Industry Application 40 (2021) 87–94.
[9] Y. Chen, Evolution of sandstone permeability under multi-field coupling, J. Cent. S. Univ. 48 (2017) 2449–2457.
[10] P. Zhang, C. Zhao, J. Hou, T. Li, X. Zhang, Experimental study on seepage characteristics of red sandstone under the coupled conditions of temperature, stress, and seepage, Chin. J. Rock Mech. Eng. 39 (2020) 1957–1974, https://doi.org/10.13722/j.cnki.jrme.2020.0229.
[11] S. You, F. Li, H. Ji, H. Wang, C. Zhang, Mechanical response linkage mechanism of deep granite under high stress and high water pressure, Journal of Chinese Coal Society 45 (2020) 219–229, https://doi.org/10.13225/j.cnki.jccs.2020.1389.

[12] L.N.Y. Wong, V. Maruvanchery, G. Liu, Water effects on rock strength and stiffness degradation, Acta Geotech 11 (2016) 713–737, https://doi.org/10.1007/s11440-015-0407-7.
[13] C. Chen, S. Peng, J. Xu, Y. Tang, D. Shang, Experimental study on stress relaxation characteristics of sandstone under the coupling of water pressure and stress, Chin. J. Rock Mech. Eng. 41 (2022) 1193–1207, https://doi.org/10.13722/j.cnki.jrme.2021.0941.
[14] J. Wu, M. Feng, W. Zhang, B. Yu, Z. Chen, G. Han, Effect of confining pressure and pore water pressure on energy consumption characteristics of saturated sandstone, Journal of Basic Science and Engineering Sciences 27 (2019) 180–193, https://doi.org/10.16058/j.issn.1005-0930.2019.01.016.
[15] Y. Zhao, J. Tang, W. Wang, G. Cheng, S. Luo, C. Fu, Study on fluid-structure coupling failure behavior of Maokou limestone under conventional triaxial compression, Journal of Mining and Safety Engineering 35 (2018) 205–212, https://doi.org/10.13545/j.cnki.jmse.2018.01.028.
[16] W. Yi, Q. Rao, Z. Li, D. Sun, Q. Shen, Thermo-hydro-mechanical-chemical (THMC) coupling fracture criterion of brittle rock, Trans. Nonferrous Met. Soc. China. 31 (2021) 2823–2835, https://doi.org/10.1016/S1003-6326(21)65696-0.
[17] Z. Luo, W. Wang, Y. Qin, J. Xiang, Early warning of rock mass instability based on multi-field coupling analysis and microseismic monitoring, Trans. Nonferrous Met. Soc. China. 29 (2019) 1285–1293, https://doi.org/10.1016/S1003-6326(19)65035-1.
[18] X. Xu, M. Karakus, F. Gao, Z. Zhang, Thermal damage constitutive model for rock considering damage threshold and residual strength, J. Cent. South Univ. 25 (2018) 2523–2536, https://doi.org/10.1007/s11771-018-3933-2.
[19] W. Li, S. Zhang, D. Deng, H. Zhao, Research on sandstone failure criteria based on energy principle, Coal science and technology 45 (2017) 70–75, https://doi.org/10.13199/j.cnki.cst.2017.12.013.
[20] S. You, X. Ming, Q. Hu, Study on failure criteria of sandstone under water-rock coupling based on energy principle, Min. Res. Dev. 38 (2018) 56–61, https://doi.org/10.13827/j.cnki.kyyk.2018.08.012.
[21] Y. Chen, P. Xiao, X. Du, S. Wang, Rafig Azam, Rock damage constitutive model based on Weibull distribution under the coupling of temperature and confining pressure, Ind. Constr. 52 (2022) 160–167, https://doi.org/10.13204/j.gyjzg21030203.
[22] B. Jin, K. Wang, W. Zhu, D. Wei, Study on damage and deterioration constitutive model of sandstone under temperature, Journal of Three Gorges University (Natural Science Edition) 40 (2018) 44–47, https://doi.org/10.13393/j.cnki.issn.1672-948x.2018.06.010.
[23] N.N. Sirdesai, A. Singh, L.K. Sharma, R. Singh, T.N. Singh, Determination of thermal damage in rock specimen using intelligent techniques, Eng. Geol. 239 (2018) 179–194, https://doi.org/10.1016/j.enggeo.2018.03.027.
[24] Y. Zhang, B. Wu, G. Zhao, Research on real-time evolution of rock thermal damage based on acoustic emission monitoring, J. Cent. S. Univ. 52 (2021) 2945–2958.
[25] K. Guo, L. Yang, X. Sheng, J. Mei, B. Li, B. Zhang, W. Yang, G. Song, Fracture mechanical behavior and acoustic emission characteristics of rock materials with three-dimensional cracks under hydraulic coupling, Rock Soil Mech. 40 (2019) 4380–4390, https://doi.org/10.16285/j.rsm.2018.2052.
[26] L. Ma, H. Sun, I. Ngo, J. Han, Infrared radiation quantification of rock damage and its constitutive modeling under loading, Infrared Phys. Technol. 121 (2022) 104044, https://doi.org/10.1016/j.infrared.2022.104044.
[27] Y. Hu, S. Yang, Z. Zhong, X. Wang, T. Zhang, R. Zhou, Experimental study on the coupling characteristics of unsaturated seepage and stress in a single fracture of limestone, Chin. J. Rock Mech. Eng. 41 (2022) 2846–2856, https://doi.org/10.13722/j.cnki.jrme.2021.0823.
[28] P. Li, Q. Rao, W. Ma, S. Su, C. Ma, Fracture analysis of thermal-hydro-mechanical coupling fracture of brittle rocks, Chin. J. Rock Mech. Eng. 33 (2014) 1179–1186, https://doi.org/10.13722/j.cnki.jrme.2014.06.011.
[29] A. He, Z. Wang, B. Chen, Research on thermal damage characteristics and mechanism of Huashan granite, Hydro-Sci. Eng. (2018) 95–101, https://doi.org/10.16198/j.cnki.1009-640X.2018.01.014.
[30] Y. Hu, Q. Wang, X. Shi, Q. Hou, Q. Zhang, J. Zhao, Influence of multi-field coupling on hydraulic fracture morphology, Pet. Geol. Oilfield Dev. Daqing 37 (2018) 82–89, https://doi.org/10.19597/j.issn.1000-3754.201710040.
[31] J. Wu, X. Chen, L. Huang, Coupled crack simulation and crack resistance prediction of early age concrete based on unified phase field theory, Chin. J. Theor. Appl. Mech. 53 (2021) 1367–1382.
[32] J. Fu, W. Chen, Y. Tan, J. Wang, W. Song, Experimental study on pore variation and Meso-damage of saturated sandstone under unloading condition, Rock Mech. Rock Eng. 56 (2023) 4669–4695, https://doi.org/10.1007/s00603-023-03293-4.
[33] L. Zhang, Z. Wang, T. Zhao, Y. Cong, Experimental study on crack propagation behavior of sandstone under the action of pore water pressure, Rock Soil Mech. 43 (2022) 901–908, https://doi.org/10.16285/j.rsm.2021.0667.
[34] M. Cai, Rock Mechanics and Engineering, China Science Publishing & Media Ltd,(CSPM), 2002. https://book.douban.com/subject/1134143/. (Accessed 28 June 2023).
[35] C.D. Martin, N.A. Chandler, The progressive fracture of Lac du Bonnet granite, Int. J. Rock Mech. Min. Sci. Geomech. Abstr. 31 (1994) 643–659, https://doi.org/10.1016/0148-9062(94)90005-1.
[36] T. Shi, J. Fu, W. Song, A Method for Establishing Three-Dimensional Random Fracture Model [P] Beijing: CN113946984B, 2022, 04-22, n.d.
[37] X. Wang, H. Xie, R. Zhang, G. Zhang, Z. Xu, J. Deng, D. Wang, C. Li, G. Feng, Z. Zhang, L. Ren, Progressive failure characterization of sandstone from Yingjinshan area in Qinghai-Tibet plateau, Rock Mech. Rock Eng. 55 (2022) 6723–6740, https://doi.org/10.1007/s00603-022-02999-1.